Plasma Physics and Controlled Fusion

PAPER

Measuring stopping power in warm dense matter plasmas at OMEGA

To cite this article: B Lahmann *et al* 2023 *Plasma Phys. Control. Fusion* **65** 095002

View the article online for updates and enhancements.

You may also like

- X-ray Thomson scattering measurement of temperature in warm dense carbon
K Falk, C L Fryer, E J Gamboa et al.
- Plasma phase transition
G E Norman and I M Saitov
- Electronic and optical properties of warm dense lithium: strong coupling effects
Jiayu Dai, Cheng Gao, Huayang Sun et al.

This content was downloaded from IP address 198.124.216.150 on 12/09/2023 at 15:28

IOP Publishing Plasma Physics and Controlled Fusion
Plasma Phys. Control. Fusion **65** (2023) 095002 (11pp) https://doi.org/10.1088/1361-6587/ace4f2

Measuring stopping power in warm dense matter plasmas at OMEGA

B Lahmann[1,*], A M Saunders[2], T Döppner[2], J A Frenje[1], S H Glenzer[3], M Gatu-Johnson[1], G Sutcliffe[1], A B Zylstra[2] and R D Petrasso[1]

[1] Massachusetts Institute of Technology, Cambridge, MA 02139, United States of America
[2] Lawrence Livermore National Laboratory, Livermore, CA 94550, United States of America
[3] Stanford University, Stanford, CA 94305, United States of America

E-mail: lahmann1@llnl.gov

Received 13 April 2023, revised 12 June 2023
Accepted for publication 6 July 2023
Published 19 July 2023

Abstract

A platform has been developed for accurately measuring the stopping power of high energy protons through warm dense matter (WDM) plasmas characterized by x-ray Thomson scattering. In this work stopping power measurements were successfully made through both WDM Beryllium and Boron plasmas. In the Boron experiments, an increase in stopping was observed over their cold target counter-parts. This increase in stopping was shown to agree well with models that account for the partial ionization of the plasma.

Keywords: warm dense matter, stopping power, partially ionized plasmas

(Some figures may appear in colour only in the online journal)

1. Introduction

Stopping power refers to the energy loss of charged particles as they traverse through matter, often expressed in differential energy loss per unit distance $\mathrm{d}E/\mathrm{d}x$ or per unit areal density $\mathrm{d}E/\mathrm{d}\rho x$. In cold matter, this energy loss is due to interactions with bound electrons for which there are several models [1–3]. In fully ionized plasmas, the energy loss is due to Coulomb collisions between the charged particle and the ions and free electrons within the substance [4]. Stopping power in these plasmas are often modeled by a binary collision theory [5, 6] or by a dielectric response theory [4, 7–9].

Stopping power is a very fundamental phenomenon in any nuclear fusion based research. This is because nuclear fusion products often are charged particles born within some source plasma. For inertial confinement fusion (ICF), the source plasma can range several orders of magnitude in density and temperature throughout the course of a single experiment [4, 10]. For this reason, accurately modeling $\mathrm{d}E/\mathrm{d}x$ in these experiments can be challenging as different theories are needed for different regimes. Overcoming this challenge is important primarily for two reasons. Firstly, many charged-particle diagnostics rely on the understanding of $\mathrm{d}E/\mathrm{d}x$ in order to interpret charged-particle spectra and infer quantities like areal density (ρR) and temperature [11–13]. Additionally, the design of high-gain ICF experiments is entirely based around the assumption that alpha particles will deposit their energy into both the hot-spot and the cold-layer of the fuel [14]. Exactly how this energy is deposited determines the hot-spot ρR required to achieve ignition and the specific dynamics of the burn-wave propagation [15].

Warm dense matter (WDM) can be understood as the state of matter between cold solids and hot plasmas. There are often two dimensionless parameters used to classify the WDM regime. The first is the degeneracy parameter:

$$\theta \equiv \frac{k_\mathrm{B}T_\mathrm{e}}{E_\mathrm{F}} \tag{1}$$

where $k_\mathrm{B}T_\mathrm{e}$ is the electron temperature and E_F is the electron Fermi energy given by:

$$E_\mathrm{F} \equiv \frac{\hbar^2}{2m_\mathrm{e}}\left(3\pi^2 n_\mathrm{e}\right)^{2/3}. \tag{2}$$

* Author to whom any correspondence should be addressed.

 © 2023 IOP Publishing Ltd

This parameter indicates whether or not the electrons of a material are Fermi degenerate. When $\theta \gg 1$ the state is considered to be non-degenerate. In this regime, the distribution of electrons is described by a Maxwellian given by the plasma temperature.

On the other hand, when $\theta \ll 1$, the material is said to be electron degenerate. In this state, the distribution of electrons is dictated by the Pauli exclusion principle. Electrons will (on average) have higher energy states than would be described by a Maxwellian. This is because the the material is so tightly bound that there are not enough available states for all the electrons to be at their lowest possible energy. Since the Pauli exclusion principle disallows two electron from occupying the same state, some portion of the population is forced to higher relative energy levels even if the kinetic temperature is relatively low [4, 9, 10].

The other parameter of interest is the coupling parameter:

$$\Gamma_e = \frac{e^2}{a\left(k_{\mathrm{B}} T_{\mathrm{e}} + E_{\mathrm{F}}\right)} \tag{3}$$

where a is the Wigner–Seitz radius given by:

$$a \equiv \left(\frac{3}{4\pi n_{\mathrm{e}}}\right)^{1/3}.$$

The coupling parameter is a ratio between the Coulomb potential energy and the sum of the electron thermal and Fermi energies. When $\Gamma_{\mathrm{e}} \ll 1$ the plasma is considered to be weakly coupled because the Coulomb energy at average distance of separation is much less than the electron energy. This describes plasmas that are hot and diffuse and are dominated by long range collective electrostatic effects.

When $\Gamma_{\mathrm{e}} \gg 1$ the material is said to be strongly coupled. Here binary collisions dominate over long ranged electrostatic effects. These materials are cold and dense [9].

WDM describes materials that are moderately degenerate ($\theta \sim 1$) and moderately coupled ($\Gamma_{\mathrm{e}} \sim 1$) which makes useful approximations, such as Maxwellian distributions, insufficient. Few models have been developed to describe it. This regime is of particular interest because the cold-layer of ICF implosions exists in this regime during the burn phase of the implosion. The regime is shown depicted in figure 1 [9].

Given the importance WDM has to understanding alpha transport in ICF experiments, a platform that can directly test stopping power in this regime is highly desirable. Previous work has demonstrated the ability to generate WDM plasma from solid density targets using the OMEGA laser [16]. Additionally stopping power measurements of WDM Be have been demonstrated using high energy protons ($v_{\mathrm{p}} \gg v_{T_{\mathrm{e}}}$) [17]. In this work, we extend this platform by accurately characterizing the generated plasmas using x-ray Thomson scattering (XRTS) [18] so as to better interpret the stopping power data. Additionally, this work has been extended to include Boron targets. We note that discrepancies between stopping power models is less significant when $v_{\mathrm{p}} \gg v_{T_{\mathrm{e}}}$, but this work still demonstrates a platform that could be extended to lower velocity probe particles.

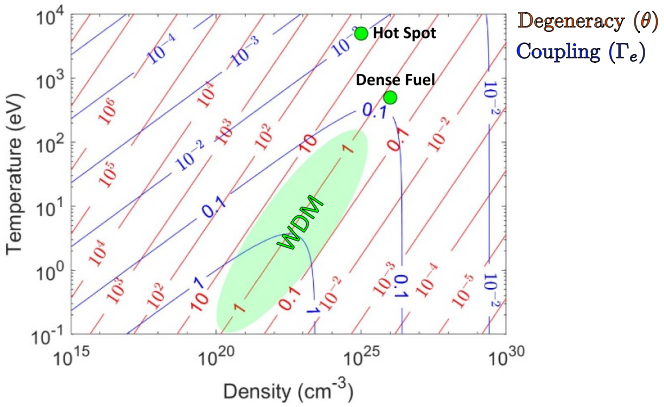

Figure 1. Depiction of where the WDM regime exists in density, temperature space. Contours shown in red and blue correspond to constant values of θ and Γ_{e} respectively. The green shaded area is generally where the WDM regime is considered to be.

2. Experimental design

In this section we will discuss the design of the WDM Target, the experimental configuration for measuring stopping power, and the experimental configuration for using XRTS.

2.1. WDM target

The WDM Target has been designed such that it can be heated to a uniform WDM plasma through which the stopping power of high energy protons can be measured. In order to accurately measure the stopping power, it is crucial that the target has a very well defined areal density (ρL). The targets are cylindrical such that the protons can probe the linear dimension whose length L was well characterized before the experiment. Additionally, the targets were solid with a well characterized density ρ. The target was heated isochorically, such that the density remained constant throughout the entire experiment.

The isochoric heating process was done through x-ray energy deposition. The OMEGA laser beams directly illuminated the radial surface of the target which was coated with an x-ray conversion material. This causes the coating material to heat and emit x-rays that penetrate through the rest of the target material, heating it uniformly and isochorically. A basic schematic of the target design is shown in figure 2.

The specific target characteristics were set by considering of the facility limitations and desired WDM plasma characteristics. The total laser energy available at OMEGA sets a limit on the atomic number (Z) of the target material. This is because fully ionizing a target of the masses required for this experiment with the OMEGA laser is very difficult for any material with $Z > 2$. If the target Z is too high, the resultant plasma

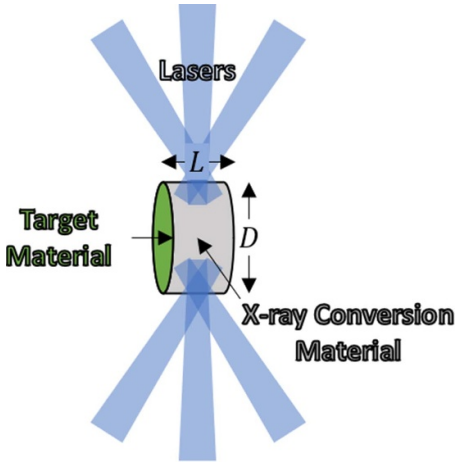

Figure 2. Basic schematic of the WDM target design. The target is a cylindrical plug with some length L and some diameter D. It is made up of some primary target material that will be heated to WDM and is coated with some x-ray conversion material that will generate x-rays when heated by the OMEGA laser.

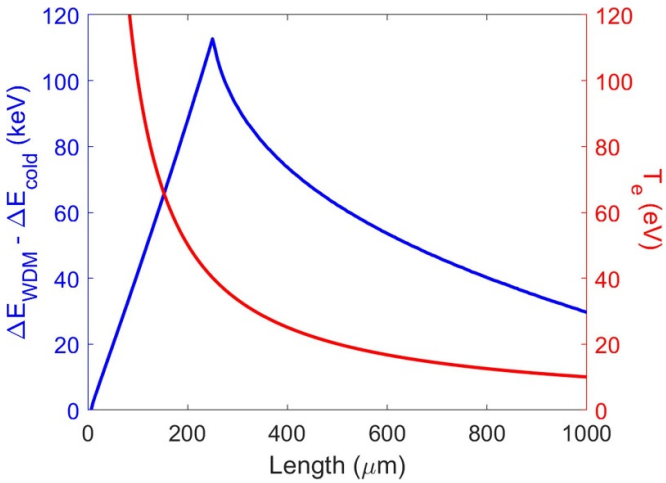

Figure 3. Estimations for the target T_e (red) and the differences between warm and cold stopping (blue) as a function of the target length. All parameters were calculated for a Be plug of diameter 800 μm illuminated by 30 OMEGA laser beams, with an assumed x-ray conversion efficiency of 1%. Energy loss was estimated using the Zimmerman Stopping Power Model. Partial ionization was estimated using the formula $Z = 20\sqrt{T_e}$. This simple formula results in a discontinuity in the stopping power differences at the temperature corresponding to $Z = 4$. The stopping power in the Zimmerman model is not sensitive to changes in T_e at these low values. As a result, the differences in stopping simply increase linearly with length up until partial ionization becomes a factor. Beyond this point, the warm stopping power tends toward the cold stopping power as the ionization tends toward 0.

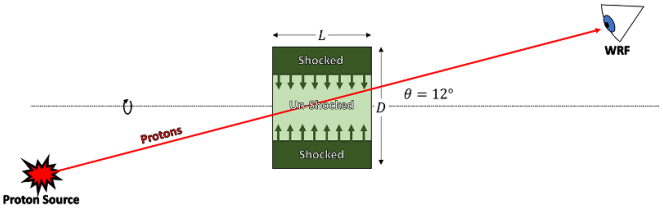

Figure 4. Schematic of the shock wave traveling through the WDM target. The shocked region is depicted as a dark green and the un-shocked region is shown as a light green. For the experiment to be successful, protons can only go through the un-shocked region where the plasma properties are well known.

will consist primarily of bound electrons which will result in stopping powers very similar to cold matter. In order to get results that are distinguishable from cold matter stopping, our target Z must be as low as possible. This points to materials such as Li, Be, B, or C. In these experiments we used both Be and B targets. The targets were coated with 2 μm of Ag and Cr respectively. The thickness was chosen based on previous experiments [17].

Additionally, the available laser energy limits both D and L. Increasing the volume (and thus total mass) of the target results in colder less ionized plasmas for a fixed amount of energy. However, the volume cannot be arbitrarily small for two separate reasons. L must be sufficiently large such that a significant amount of energy (ΔE) is lost by the protons probing the plasma. The uncertainty on ΔE is somewhat fixed around 50 keV by the systematic uncertainty of the detectors and counting statistics. We therefore want $\Delta E \gg 50$ keV to ensure that our measurement is significant. Additionally, the difference in stopping measured between cold matter and WDM must also be greater than 50 keV. This difference decreases as L gets large due to the aforementioned effects of increasing the volume. Figure 3 shows these trade offs and optimization as a function of length for a Be target.

When the lasers illuminate the circular surface of the plug, a shock wave is launched inward toward the center of the plug. The density and temperature behind the shock-wave are difficult to characterize accurately and therefore are undesirable plasma properties to probe. To avoid this, we must probe the un-shocked (yet still x-ray heated) region far before the shock can reach it. Figure 4 shows a schematic of this requirement.

As seen in figure 4, the protons probe the target at an angle $\theta = 12°$. This is because the target is oriented such that it would be lined up with the crystal of the x-ray spectrometer used in the XRTS configuration discussed in section 2.3. The crystal was offset 12° from the x-ray spectrometer which was fielded in the same location as the proton spectrometer (not simultaneously). It was important to maintain this orientation so that the laser drive on the WDM target used in the different shot configurations would be identical. As a result of this, the protons probe radii between 0 to $(L/2)\sin\theta$. Meanwhile the shock-wave travels inward at some velocity similar to the sound speed c_s of the material. This creates the requirement that:

$$D \gg L\sin\theta + 2c_s\tau \tag{4}$$

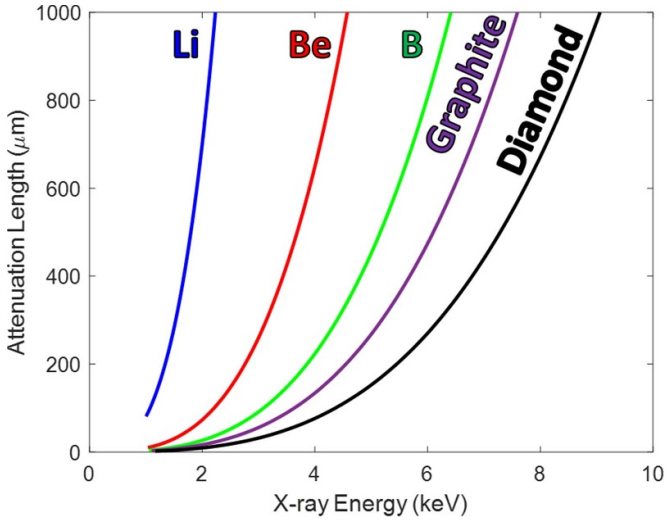

Figure 5. X-ray attenuation lengths for various low Z target materials. The blue, red, green, purple, and black curves correspond to a Li, Be, B, graphite, and diamond target respectively.

where $\tau \sim 1.5$ ns is the time between the lasers hitting the target and the protons leaving the target. The exact value of the minimum diameter depends on many variables, but generally resolves to be of order 200–300 μm.

The x-ray conversion material is selected based on atomic line spectral energies due to laser heating and the target material. Optimally, the dominant x-ray line emission energy would have an attenuation length on the order of D; x-ray energies of attenuation lengths much lower than D will result in a non-uniform temperature profile because the x-rays will not fully attenuate through the target whereas x-rays with much larger attenuation lengths will not deposit a significant amount of energy into the target, decreasing the total efficiency. Figure 5 shows the attenuation lengths as a function of x-ray energy for several proposed target materials. As shown, attenuation length is a function of both target material atomic number and material density. Considering a standard OMEGA-scale target with dimensions on the order of several hundreds of microns, optimal x-ray energies range from approximately 1 to 9 keV. In our experiments the Be targets were coated with Ag and the B targets were coated with Cr.

Another thing to consider when choosing the x-ray conversion material is the x-ray Thomson Scattering backlighter material. The plasma must be characterized using x-ray Thomson Scattering which requires it is own x-ray source. The details of this are discussed later in section 2.3. The energy of x-ray line emission used for the XRTS measurement must be adequately separated from the energy of the heating source in order not to obfuscate scattered x-ray energy interpretation.

2.2. Proton source configuration

In order to measure the stopping power, high energy protons must be generated to probe the WDM material. For this we use a D^3He backlighter located 10 mm away from the WDM plasma. For our experiments the backlighter was a 18 atm 50/50 D^3He filled capsule. The nominal OD was 860 μm and the nominal shell thickness was 2.0 μm of SiO_2. These dimensions were chosen to ensure a sufficient proton yield for the experiments.

The proton backlighter and the WDM Target must be lined up along the line of sight of a charged particle spectrometer. In our experiments, wedge range filters (WRFs) [12, 13, 19] were used for this purpose.

Another important part of the experiment involves characterization of the proton source spectrum, which we accomplish by fielding additional WRFs. The energy of the protons emitted have been demonstrated to be independent of the line of sight meaning the placement of these WRFs is fairly arbitrary. In our experiments, several WRFs were fielded along multiple lines of sight so that this assumption could be verified *in-situ*.

Finally, the timing of the proton emission is important. As previously mentioned, the experiment is designed such that the protons will probe the WDM target at some $\tau \sim 1.5$ ns after the onset of the laser drive. This ensures that electrostatic charging effects are minimal at the time of probing [17].

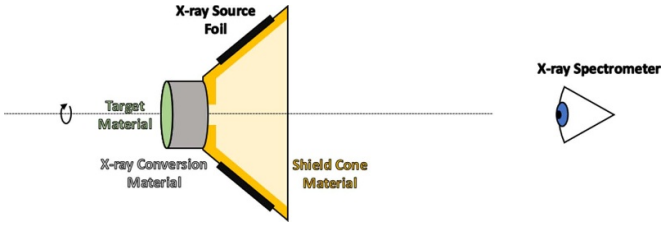

Figure 6. Schematic of the x-ray Thomson Scattering configuration. Note that the cone (gold color) is hollow, allowing for x-rays to scatter back into the x-ray spectrometer.

2.3. X-ray Thomson scattering configuration

We use x-ray Thomson scattering to characterize the ionization level and temperature of our plasma, as has been demonstrated in several warm dense matter experiments [16, 20–25]. For this technique to work, x-rays need to scatter within the plasma volume at a well defined angle into an x-ray spectrometer. The characteristics of the scattered x-ray spectra gives information about the plasma characteristics.

To achieve this, a x-ray foil was placed onto a cone attached to the axial face of the WDM target. The cone serves two purposes; its angle defines the scattering angle of the x-rays and also shields the spectrometer from the direct emission of the foil. A schematic of this configuration is shown in figure 6.

As seen in figure 6, a shielding cone blocks the spectrometer's direct line of sight to the XRTS source x-rays. Because of its role as an x-ray shield, the cone material must be made out of some high-Z material. In our experiments both gold and tantalum was used for this role. Similarly to the considerations of the heater material, x-ray line emission energies of the

shield must lie well away from energies needed for the XRTS measurements, as shield material has the potential to heat and radiate in response to heating x-rays. In our experiments both Au and Ta were used. It should also be noted that the shield cone has a collimator where it contacts the primary target. This is to shield the spectrometer from x-rays that scatter in the shocked region of the plasma. This collimator must have some diameter D_c less than D by at least $2c_s\tau$. Like before, the exact value of $2c_s\tau$ varies, but tends to be of order 100–200 μm. Our experiment used a 400 μm diameter for the collimator.

The addition of this shield cone is not expected to have any impact of the probed plasma conditions. This is because no lasers directly interact with the shield cone to generate any additional sources of heat. The cone is also placed such that it does not inhibit x-rays from the converter from reaching the WDM Target. This is important because the proton source configuration and the x-ray Thomson Scattering configuration describe two distinct experiments. The two configurations were performed alternatively on subsequent shots to avoid diagnostic interference.

2.4. Hydrodynamics simulation

A 1D hydro simulation was performed in Helios [26] to verify the uniformity of the plasma conditions in the region probed by both the high energy protons and the XRTS measurements. This simulation was done for an 860 μm diameter Cr coated boron plug. In this simulation the laser drive was tuned (reduced) to match the observed electron temperatures discussed in section 3 [25]. The calculated densities and temperatures are shown plotted in figures 7 and 8 respectively. This simulation shows that the density and temperature are uniform in the region probed by the XRTS measurements. The protons integrate much less time than the XRTS measurement and for a target of length 500 μm the protons probe radii less than $\sim$100 μm. This means that the protons see the same uniform conditions as the XRTS measurements. Note also that the electron temperature does not change significantly after the laser is turned off at 1 ns. This means that the time integrated XRTS measurement is representative of the temperatures seen by the protons at $\tau \sim 1.5$ ns. Similar conclusions were drawn from 2D LASNEX [27] simulations performed for a previous iteration of this platform [16].

3. Results

The results consist of 12 different OMEGA shots all listed in table 1. These experiments include the measurement of stopping power in cold Be, WDM Be, cold Boron, and WDM Boron. Also included are XRTS experiments used to characterize the plasma properties of the WDM plasmas. Example downshifted spectra are shown in figure 9 and all downshifted spectra are shown in figure 16. The XRTS spectra for WDM Be and Boron are shown in figures 10 and 11 respectively.

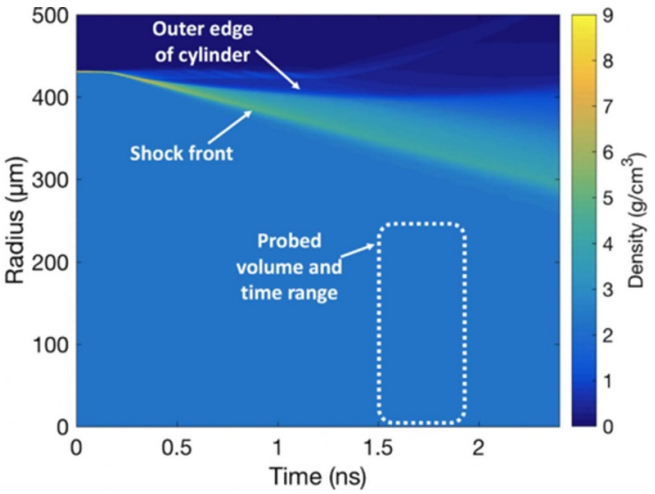

Figure 7. Simulated density of a Cr coated boron plug driven by a 1 ns square pulse as a function of radius and time. The region probed by the XRTS measurement is shown in the area enclosed by the white dashed line. This simulation shows that the boron plug maintains it is solid density within the region probed by the XRTS measurement. For these experiments protons would probe the target at $\tau \sim 1.5$ ns between radii less than 100 μm. Reprinted (figure) with permission from [25], Copyright (2018) by the American Physical Society.

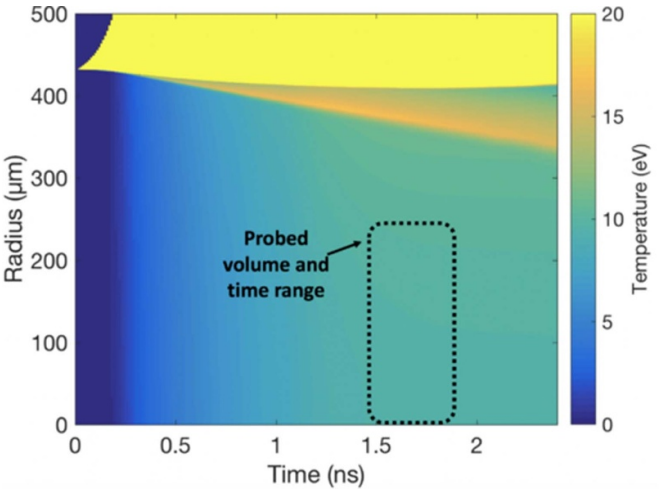

Figure 8. Simulated electron temperature of a Cr coated boron plug driven by a 1 ns square pulse as a function of radius and time. The region probed by the XRTS measurement is shown in the area enclosed by the black dashed line. This simulation shows that the electron temperature stays relatively constant after the laser turns off at 1 ns. As a result, the region and time integrated by the XRTS measurement is of one uniform electron temperature. For these experiments protons would probe the target at $\tau \sim 1.5$ ns between radii less than 100 μm. Reprinted (figure) with permission from [25], Copyright (2018) by the American Physical Society.

As mentioned in section 2.2, several WRFs were fielded around the OMEGA chamber during the stopping power

Table 1. table of all of the shots conducted in these experiments. Shots labeled as Cold indicate an experiment where the target material was not driven. Those labeled Warm indicate experiments where the target material was heated to WDM.

Shot number	Target material	Cold/Warm	Configuration
82293	Ag coated Be	Cold	dE/dx
82291	Ag coated Be	Warm	dE/dx
82295	Ag coated Be	Warm	dE/dx
82290	Ag coated Be	Warm	Gold Cone XRTS
82294	Cr coated Boron	Cold	dE/dx
88649	Cr coated Boron	Cold	dE/dx
88650	Cr coated Boron	Cold	dE/dx
82292	Cr coated Boron	Warm	dE/dx
88651	Cr coated Boron	Warm	dE/dx
88652	Cr coated Boron	Warm	dE/dx
88653	Cr coated Boron	Warm	dE/dx
88647	Cr coated Boron	Warm	Tantalum Cone XRTS

measurements. The source spectrum was measured from four WRFs along two distinct line of sights to verify source uniformity. In the analysis, each source spectrum was separately fitted with a normal distribution and the mean was taken to be the birth energy. The final birth energy used in the downshift analysis was taken to be the average of these means. Example source spectra are shown plotted in black in figure 9. The primary source of uncertainty in this analysis was the systematic uncertainties in the calibration of the WRFs.

The downshifted spectrum was measured by a single WRF positioned opposite the proton source with the WDM target positioned in-between. For the downshift analysis, a normal distribution was fitted to the downshifted peak and the mean was taken to be the downshifted energy. For the cold experiments (experiments where the WDM target was not driven by lasers), the downshifted spectra looked exactly as expected; lower in energy and broader than the source spectrum. For the warm experiments, these characteristics were also observed however the source spectrum was also present in the WRF data. While this source spectrum agreed well with the other measurements, it is mean value was not used in the analysis. It is unclear how the WRF measured both the source and downshifted spectrum. One theory is that magnetic fields generated around the WDM target were able to bend protons around the WDM target onto the WRF. If this is true, the fact that the source spectrum agrees well with other measurements imply that no significant electric fields affected the protons near the WDM target.

The plasma conditions of the plasma were inferred using dedicated XRTS shots. The measured XRTS spectra are sensitive both to ionization and temperature. Note that we consider mass density fixed at solid density as a characteristic for isochoric heating. As the fitting sensitivity plots in figures 10 and 11 show, the elastic feature is most sensitive to the ionization state of the material. In fitting these spectra, any ionization into the K-shell of both boron and beryllium causes the ratio of the elastic to the inelastic feature to diverge quickly

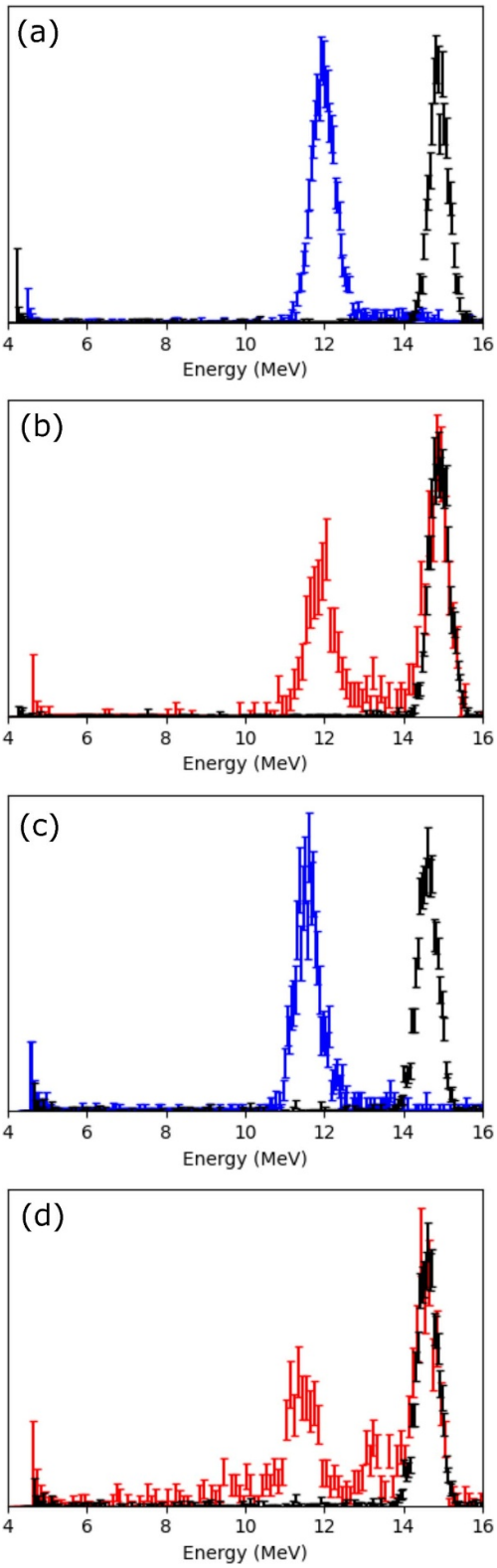

Figure 9. Example WRF D^3He proton data. Each figure shows the measured source spectrum in black and the resultant down-shifted spectrum in blue or red to indicate a cold or warm target respectively. Figure (a) corresponds to ranging through cold Be, (b) corresponds to ranging through heated Be, (c) corresponds to ranging through cold Boron, and (d) corresponds to ranging through heated Boron.

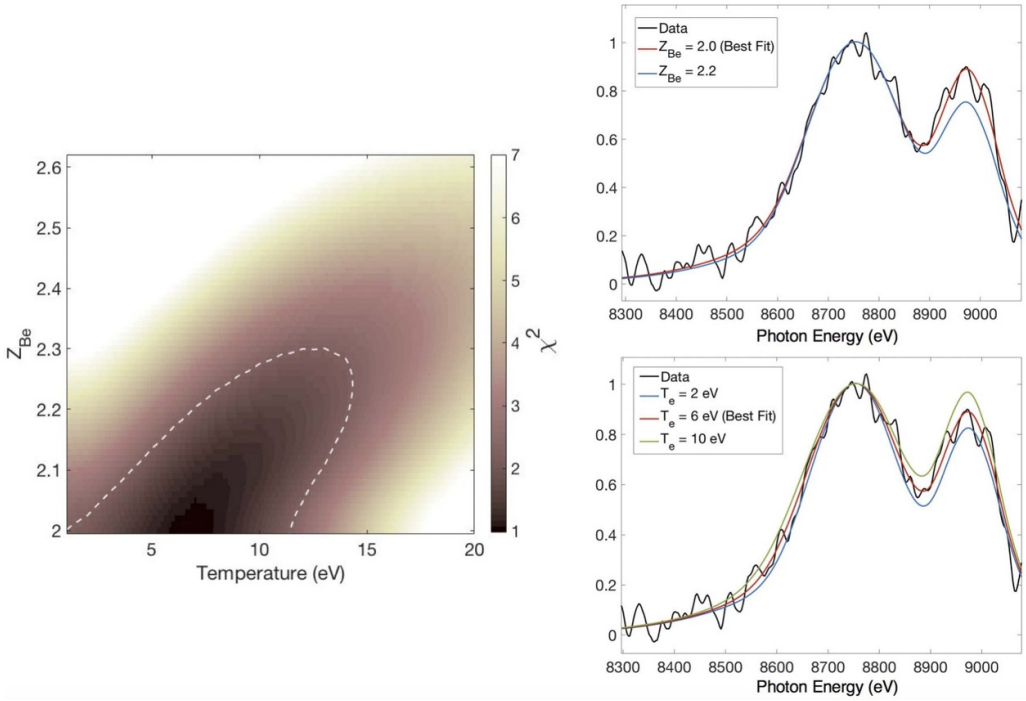

Figure 10. Left: a χ^2 map versus electron temperature and Be ionization state from OMEGA shot 82290. 1σ confidence intervals are marked by the white dashed curve. The best fit is found at a temperature of $T_e = 6^{+5}_{-5}$ eV with $Z_{Be} < 2.2$ Right: an illustration of ionization sensitivity (top right) and temperature sensitivity (bottom right) in the fitting. Both plots show the data and the best fit, as well as one or two other modeled spectra that vary ionization and electron temperature, respectively. Reprinted (figure) with permission from [25], Copyright (2018) by the American Physical Society.

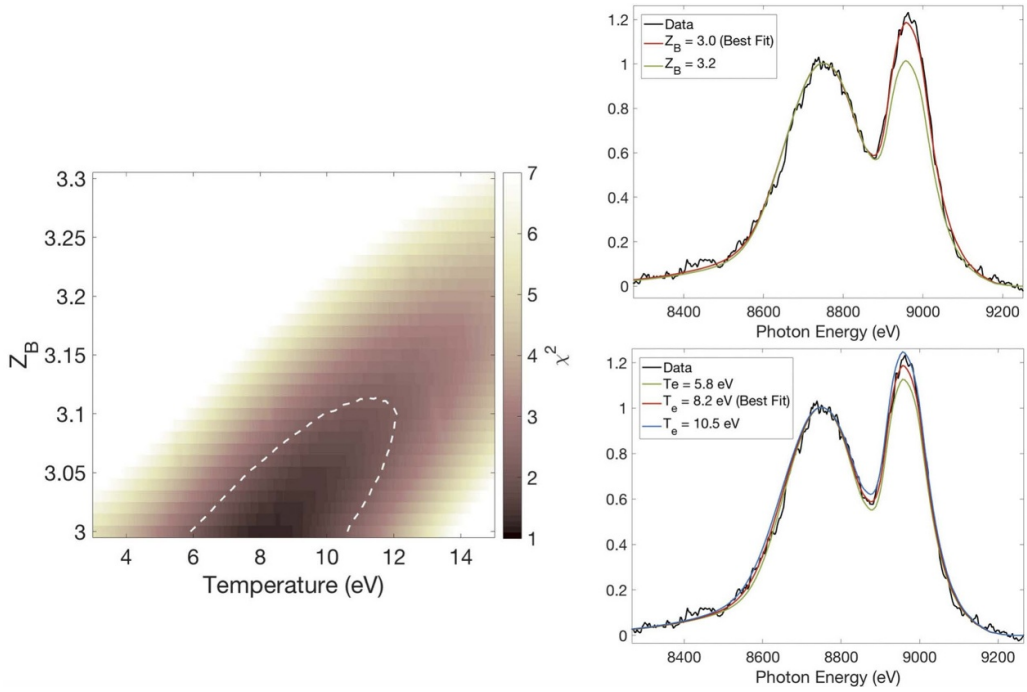

Figure 11. Left: a χ^2 map versus electron temperature and B ionization state from OMEGA shot 88 647. 1σ confidence intervals are marked by the white dashed curve. The best fit is found at a temperature of $T_e = 8.6^{+2.7}_{-3.1}$ eV with $Z_B < 3.1$ Right: an illustration of ionization sensitivity (top right) and temperature sensitivity (bottom right) in the fitting. Both plots show the data and the best fit, as well as one or two other modeled spectra that vary ionization and electron temperature, respectively. Reprinted (figure) with permission from [25], Copyright (2018) by the American Physical Society.

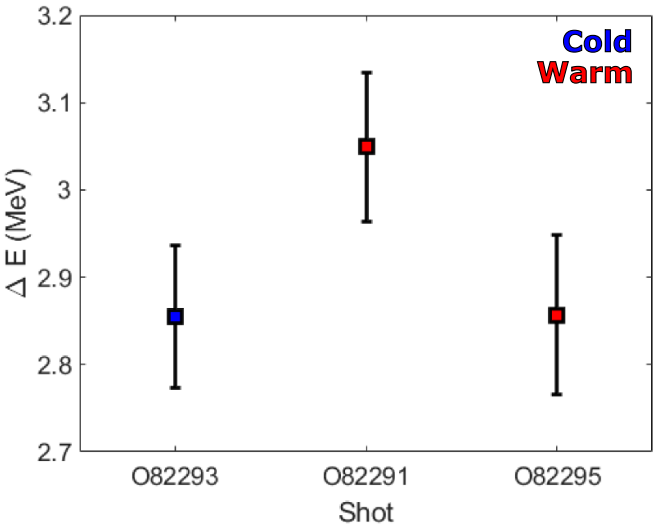

Figure 12. All of the stopping power data from Be targets. There are a total of one cold shot (blue) and two WDM shots (red). The effective areal density seen by the protons was the same for each shot at $\rho L = 101\,\mathrm{mg\,cm^{-2}}$. The XRTS inferred $T_\mathrm{e} = 6 \pm 5\,\mathrm{eV}$ and $Z < 2.2$ for the warm shots. No significant difference is observed between the cold and warm shots.

from the values observed in the data. This fact, combined with the assumed stability of the K-shells and low energies of the L-shells, allow the ionization state to be set such that the atoms each retain their two K-shell electrons. Then, the spectrum can be fit as a function of electron temperature. Variations in electron temperature cause the width of the inelastic feature to change, and as such, sum with the elastic feature to change the apparent ratio of elastic to inelastic scattering. Thusly, the apparent height of the elastic feature is a primary feature in fitting for temperature. However, the red-end of the inelastic feature also shows sensitivity to temperature and fitting of the inelastic feature alone returns the same optimal temperature, albeit with larger uncertainty bounds due to the lower number of fitting points.

As seen in figure 10, the WDM Be was heated to an electron temperature of $T_\mathrm{e} = 6^{+5}_{-5}\,\mathrm{eV}$ with an ionization of $Z_\mathrm{Be} < 2.1$. One quantity of interest is the velocity projectile ratio ($v_{T_\mathrm{e}}/v_\mathrm{p}$) where v_{T_e} is the thermal velocity of the electrons in the plasma and v_p is the velocity of the particle traversing the plasma. At this electron temperature, $v_{T_\mathrm{e}}/v_\mathrm{p}$ goes from 2.7% to 3.0% as the proton transverses the plasma. This temperature is lower than what was inferred in previous work [17, 20]. As a result, we expect the stopping power of this WDM plasma to be very near that of cold matter. This is confirmed by the data shown in figure 12. While a slight enhancement in stopping appears to be present, the difference is not statistically significant.

Despite this, we compare our measurement with the expectations of the stopping power models in figure 13. Here we compare the data with the BPS [8] and Zimmerman [28]. The BPS model combines stopping from both binary collisions and dielectric response with an additional quantum correction on both terms. The Zimmerman model is a parameterization of the Maynard–Deutsch theory [7] (a dielectric response model) that also includes a treatment for partial ionization effects. It is shown that the data is well modelled by the Zimmerman stopping power model when the effects of partial ionization

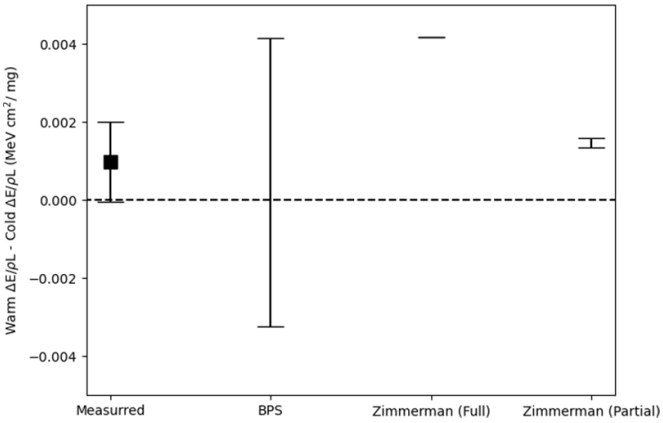

Figure 13. Comparison of various stopping power models to the measured difference between warm and cold stopping in Be. The plotted data point is the average warm stopping (of two shots) subtracted from the single cold stopping power measurement. BPS matches the observed data due to the large error in the electron temperature measurement. Zimmerman matches the data well only when the effects of partial ionization are considered. This demonstrates the importance of partial ionization in these WDM plasmas.

are considered. In this model, 38.6% of the stopping is due to the bound electrons. Assuming full ionization over predicts the difference between warm and cold. BPS also matches the observed data but the large relative error in the electron temperature results in very large errors in the model. The error bars are determined by propagating the electron temperature and ionization uncertainties through the individual stopping power models.

For the WDM Boron, figure 11 shows that we inferred an electron temperature of $T_\mathrm{e} = 8.6^{+2.7}_{-3.1}\,\mathrm{eV}$ with an ionization of $Z_\mathrm{B} < 3.1$. At this electron temperature, $v_{T_\mathrm{e}}/v_\mathrm{p}$ goes from 3.3% to 3.8% as the proton transverses the plasma. This temperature also is smaller than was inferred in previous work

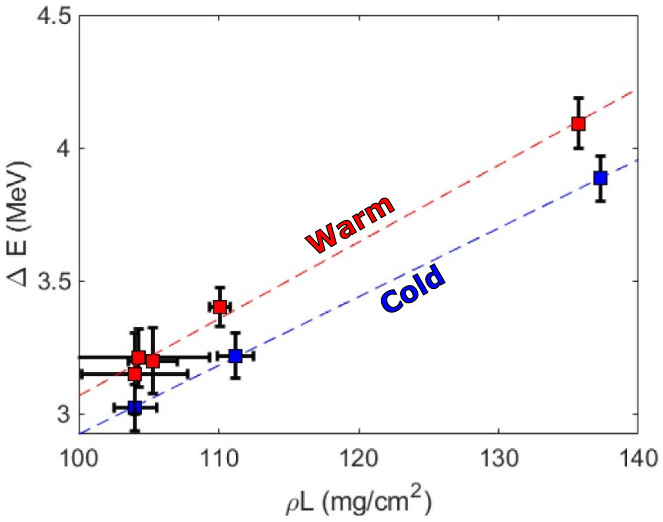

Figure 14. All of the stopping power data from Boron targets. There were a total of three cold shots (blue) and five WDM shots (red). The areal density of each target varied due to manufacturing differences. The XRTS inferred $T_e = 8.6^{+2.7}_{-3.1}$ eV and $Z < 3.1$ for the warm shots.

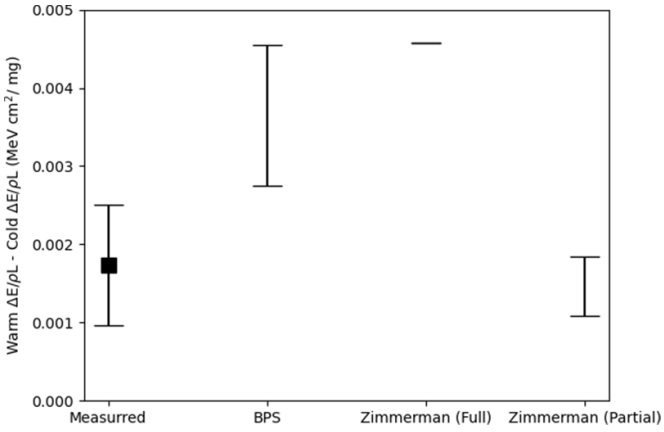

Figure 15. Comparison of various stopping power models to the measured difference between warm and cold stopping in Boron. The plotted data point is the average warm stopping power (of five shots) subtracted from the average cold stopping power (of three shots). BPS and Zimmerman overshoot the measurement when they do not account for the effects of partial ionization. The Zimmerman model agrees well once partial ionization is included. For all of the models SRIM is used to model the cold measurement.

but is significantly hotter than what was achieved with the Be targets. As a result, we expect a more significant increase in stopping between warm and cold Boron. This is confirmed by data shown in figure 14. This figure is plotted as a function of areal density because the length of the boron targets varied significantly from shot to shot due to target fabrication difficulties. These difficulties stemmed from challenges with cutting the raw material. Additionally, the target specifications of these experiments allowed for the length to vary significantly. With more care and effort, it is possible to make boron targets of more equal length.

The discrepancy in temperatures between the Be and B targets are thought to be due to a poor understanding of the x-ray converter. The laser intensities were optimized for uniformity without taking x-ray conversion efficiency into account. Additionally the x-ray conversion materials were chosen based on their lines and not on any data regarding x-ray conversion efficiencies.

Like with the Be, we compare the stopping of WDM Boron with the BPS and Zimmerman stopping power models in figure 15. Like before, the Zimmerman stopping power model reproduces the measured value well when the effects of partial ionization are considered. In this model, 31.1% of the stopping is due to the bound electrons. The difference between warm and cold is over predicted when full ionization is assumed. The BPS stopping power model also over predicts the difference likely due to the fact that it assumes full ionization.

Our data shows that the effects of partial ionization play an important role in calculating the stopping power in WDM plasmas. Assuming full ionization in these plasmas will overpredict the total stopping due to the fact that charged particles will lose more energy to free electrons than bound electrons [4]. The data is well modeled by the Zimmerman model that treats the stopping of bound electrons and free electrons separately. This is in good agreement with what was seen in previous work with Be [17].

4. Conclusions

In this work, we have successfully expanded an existing platform to measure the stopping power of high energy protons in WDM plasmas characterized by XRTS. WDM plasmas on Be and Boron just below 10 eV were demonstrated. The stopping power of these targets were measured and shown to have increases relative to cold matter stopping when the temperatures and ionization are high enough. These differences were shown to be in good agreement with the Zimmerman stopping power model when the effects of partial ionization are correctly considered.

Future work should consider Li targets if considered feasible from a manufacturing standpoint. Work should also be done to improve the efficiency of the heating drive to push to higher temperatures and ionization states. Finally, future implementations may consider lower velocity probe particles to investigate regimes where stopping power models are more discrepant.

Data availability statement

All data that support the findings of this study are included within the article (and any supplementary files).

Appendix. Measured spectra

Below in figure 16 are all the measured downshifted spectra from the experiments listed in table 1. Spectra from shots where the target was driven are red whereas spectra from shots where the target was not driven are in blue. Each spectrum includes a source spectrum in black for reference.

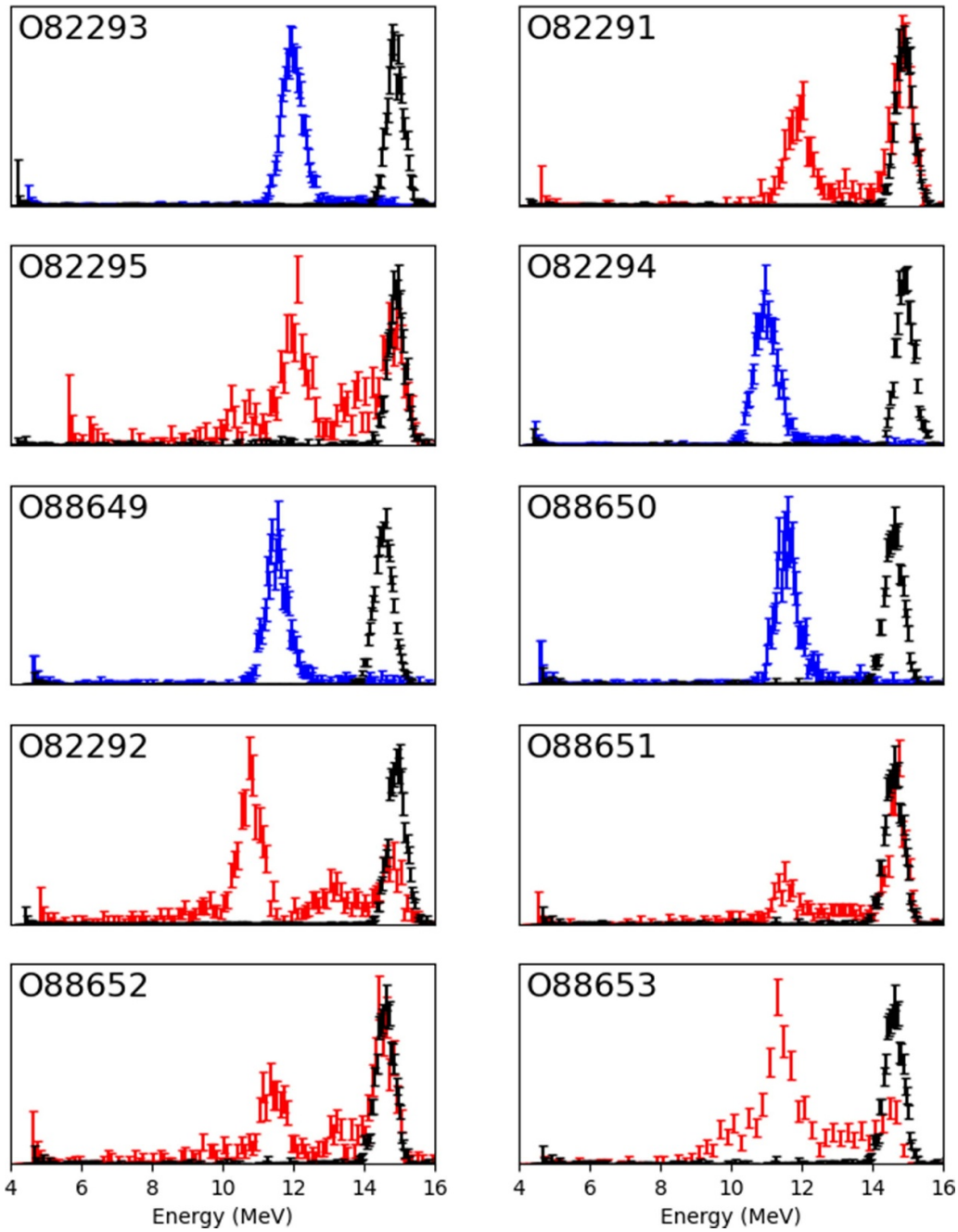

Figure 16. All downshifted spectra used in the results of this paper. Spectra plotted in red are downshifted through WDM whereas spectra in blue are downshifted through cold matter. Each plot contains a source spectrum plotted in black.

ORCID iDs

B Lahmann https://orcid.org/0000-0002-4599-8463
J A Frenje https://orcid.org/0000-0001-6846-0378
S H Glenzer https://orcid.org/0000-0001-9112-0558
A B Zylstra https://orcid.org/0000-0003-0489-7479

References

[1] Bethe H and Ashkin J 1953 Transport of radiation through the matter *Experimental Nuclear Physics* (Wiley)
[2] Bloch F 1933 Zur bremsung rasch bewegter teilchen beim durchgang durch materie *Ann. Phys., Lpz.* **408** 285–320
[3] Ziegler J F, Biersack J P and Ziegler M D 2015 *The Stopping and Range of Ions in Matter* (SRIM Company)
[4] Atzeni S and Meyer-ter Vehn J 2004 *The Physics of Inertial Fusion: Beam Plasma Interaction, Hydrodynamics, Hot Dense Matter* (*Oxford Science Publications* vol 125) (Oxford University Press) oCLC: ocm55883769
[5] Trubnikov B 1965 Particle interactions in a fully ionized plasma *Rev. Plasma Phys.* **1** 105
[6] Li C-K and Petrasso R D 1993 Charged-particle stopping powers in inertial confinement fusion plasmas *Phys. Rev. Lett.* **70** 3059–62
[7] Maynard G and Deutsch C 1982 Energy loss and straggling of ions with any velocity in dense plasmas at any temperature *Phys. Rev.* A **26** 665

[8] Brown L, Preston D and Singleton R L Jr 2005 Charged particle motion in a highly ionized plasma *Phys. Rep.* **410** 237–333
[9] Zylstra A B 2015 Using fusion-product spectroscopy to study inertial fusion implosions, stopping power, and astrophysical nucleosynthesis at OMEGA and the NIF *PhD Thesis* Massachusetts Institute of Technology
[10] Drake R P 2006 *High-Energy-Density Physics: Fundamentals, Inertial Fusion and Experimental Astrophysics* (*Shock Wave and High Pressure Phenomena*) (Springer)
[11] Hicks D G, Li C K, Petrasso R D, Séguin F H, Burke B E, Knauer J P, Cremer S, Kremens R L, Cable M D and Phillips T W 1997 Design of an electronic charged particle spectrometer to measure $\langle \rho R \rangle$ on inertial fusion experiments *Rev. Sci. Instrum.* **68** 589–92
[12] Séguin F H *et al* 2003 Spectrometry of charged particles from inertial-confinement-fusion plasmas *Rev. Sci. Instrum.* **74** 975–95
[13] Zylstra A B *et al* 2012 Charged-particle spectroscopy for diagnosing shock ρ R and strength in NIF implosions *Rev. Sci. Instrum.* **83** 10D901
[14] Lindl J 1995 Development of the indirect-drive approach to inertial confinement fusion and the target physics basis for ignition and gain *Phys. Plasmas* **2** 3933–4024
[15] Zylstra A B and Hurricane O A 2019 On alpha-particle transport in inertial fusion *Phys. Plasmas* **26** 062701
[16] Glenzer S H, Gregori G, Rogers F J, Froula D H, Pollaine S W, Wallace R S and Landen O L 2003 X-ray scattering from solid density plasmas *Phys. Plasmas* **10** 2433–41
[17] Zylstra A *et al* 2015 Measurement of charged-particle stopping in warm dense plasma *Phys. Rev. Lett.* **114** 215002
[18] Glenzer S H *et al* 1999 Thomson scattering from laser plasmas *Phys. Plasmas* **6** 2117–28
[19] Seguin F H *et al* 2012 Advances in compact proton spectrometers for inertial-confinement fusion and plasma nuclear science *Rev. Sci. Instrum.* **83** 10D908
[20] Glenzer S H, Gregori G, Lee R W, Rogers F J, Pollaine S W and Landen O L 2003 Demonstration of spectrally resolved x-ray scattering in dense plasmas *Phys. Rev. Lett.* **90** 175002
[21] Kritcher A L, Döppner T, Fortmann C, Ma T, Landen O L, Wallace R and Glenzer S H 2011 In-flight measurements of capsule shell adiabats in laser-driven implosions *Phys. Rev. Lett.* **107** 015002
[22] Lee H J *et al* 2009 X-ray thomson-scattering measurements of density and temperature in shock-compressed beryllium *Phys. Rev. Lett.* **102** 115001
[23] Falk K, Fryer C L, Gamboa E J, Greeff C W, Johns H M, Schmidt D W, Šmíd M, Benage J F and Montgomery D S 2016 X-ray thomson scattering measurement of temperature in warm dense carbon *Plasma Phys. Control. Fusion* **59** 014050
[24] Glenzer S H and Redmer R 2009 X-ray thomson scattering in high energy density plasmas *Rev. Mod. Phys.* **81** 1625–63
[25] Saunders A M, Lahmann B, Sutcliffe G, Frenje J A, Falcone R W and Döppner T 2018 Characterizing plasma conditions in radiatively heated solid-density samples with x-ray thomson scattering *Phys. Rev.* E **98** 063206
[26] MacFarlane J, Golovkin I and Woodruff P 2006 HELIOS-CR—A 1-D radiation-magnetohydrodynamics code with inline atomic kinetics modeling *J. Quant. Spectrosc. Radiat. Transfer* **99** 381–97
[27] Zimmerman G, Kershaw D, Bailey D and Harte J 1977 LASNEX code for inertial confinement fusion *Conf.: Topical meeting on inertial confinement fusion* (*San Diego, CA, USA, 7 Feb 1978*) UCRL-80169
[28] Zimmerman G B 1990 Recent developments in Monte Carlo techniques Lawrence Livermore National Lab *Technical Report* UCRL-JC-105616 (available at: www.osti.gov/biblio/6146095)